Chapter 9
High-Accuracy Thermo-Elastic Simulation on Massively Parallel Computer

Andreas Naumann, Florian Stenger, Axel Voigt and Jörg Wensch

Abstract Subproject A07 develops and explores numerical methods and techniques to implement them to solve problems in connection with thermo-elastic subassemblies' and machine tools' simulation in the CRC/Transregio 96. For this purpose, high-resolution discretization methods were developed, tested and applied both for high resolution discretization in space and for efficient integration in the long term.

9.1 Introduction

The goal of this subproject entails the development of efficient methods to simulate the thermo-elastic performance of machine tools or their subassemblies under real load conditions. Modelling and parameter setting approaches covering the entire system of the machine tool and used for the validation of several techniques for model reduction are developed. A milling machine column and a spindle are chosen as exemplary subassemblies (see Fig. 9.1, Chap. 1). The geometry of both parts is represented by a CAD model. The spindle moves up and down at a given speed. Frictional heat emitted along the line of contact makes the machine tool designers interested in understanding the heat distribution within the machine tool and the resulting deformation.

A. Naumann (✉) · F. Stenger · A. Voigt · J. Wensch
Institut für Wissenschaftliches Rechnen, TU Dresden, 01062 Dresden, Germany
e-mail: andreas.naumann@tu-dresden.de

F. Stenger
e-mail: florian.stenger@tu-dresden.de

A. Voigt
e-mail: axel.voigt@tu-dresden.de

J. Wensch
e-mail: joerg.wensch@tu-dresden.de

K. Großmann (ed.), *Thermo-energetic Design of Machine Tools*,
Lecture Notes in Production Engineering, DOI 10.1007/978-3-319-12625-8_9

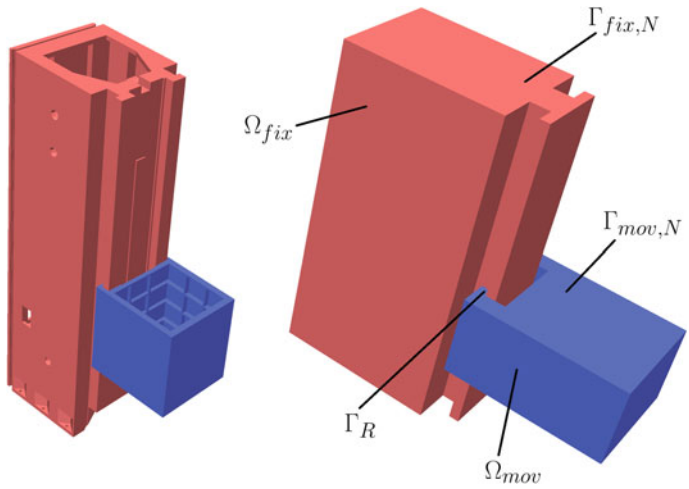

Fig. 9.1 The tool's original geometry (*left*) and the simplified geometry used for different simulation approaches (*right*). A spindle (*blue*, Ω_{mov}) and a column of a milling machine (*red*, Ω_{fix}) is shown, the spindle moves up and down the column. Neumann boundaries $\Gamma_{\cdot,N}$ are denoted and the contact line $\Gamma_R = \overline{\Omega}_{fix} \bigcap \overline{\Omega}_{mov}$

Two mathematical approaches are taken into account for the phenomena described above:

- Two different geometries, which are given independently, are sliding against each other during the process. This leads to a contact problem with varying contact conditions, which have to be considered numerically. Two different approaches will be compared. A diffuse domain approach, introduced in Li et al. (2009), in which the geometries and therefor also the contact area, are only implicitly described by a phase-field function on one global discretization, and a direct approach, in which the contact area is explicitly computed in each time step and an interpolation between two different meshes is used to deal with the heat exchange along the contact area. The different method and their comparison on a simplified geometry are described in Sect. 9.2.2.
- In the reference problem, the thermo-elastic machine tool behaviour was simulated over a period of 15 h. Here, the spindle head's movement occurs periodically in one-hour time increments, with periods from 1.5 to 48 s. The periods and velocities are shown in Table. 9.1. The timescale of the periods is clearly shorter than that of the integration. Section 9.2.3 deals with an approach that makes use of this periodicity in temporal integration. For numerical simulation, defect corrected averaging employs a replacement problem identified as suitable, which precisely approximates the solution in stroboscopic spaces.

Table 9.1 Velocities and corresponding periods

h	1	2	3	4	5	6	7	8	9	10	11	12	13	14	15
v (m/min)	2.5	2.5	2.5	5	5	5	10	10	10	15	15	15	20	20	20
Period (s)	12	48	12	6	24	6	3	12	3	2	8	2	1.5	6	1.5

9.2 Approaches

9.2.1 Mathematical Model for Heat Exchange

On the two domains Ω_{fix} and Ω_{mov}, where the first one is fixed and the second one represents the moving part, two temperatures T_{fix} and T_{mov} have to be considered. The equations read:

$$\rho c_p \partial_t T_{fix} - k\Delta T_{fix} = 0 \quad \text{in} \quad \Omega_{fix} \tag{9.1}$$

$$\rho c_p(\partial_t T_{mov} + \nabla \cdot (\mathbf{v} T_{mov}) - b\Delta T - mov = 0 \quad \text{in} \quad \Omega_{mov}(t) \tag{9.2}$$

where ρ is the materials density, c_p the specific heat capacity and k the thermal conductivity. $\mathbf{v}$ is the given velocity of the moving part. The boundary conditions

$$\nabla T_{fix} \cdot \mathbf{n} = 0 \quad \text{on } \Gamma_{fix,N}(t) \tag{9.3}$$

$$\nabla T_{fix} \cdot \mathbf{n} = \alpha(T_{fix} - T_{mov}) + \frac{\eta}{2} \qquad \text{on } \Gamma_R(t) \tag{9.4}$$

$$\nabla T_{mov} \cdot \mathbf{n} = 0 \quad \text{on } \Gamma_{mov,N}(t) \tag{9.5}$$

$$\nabla T_{mov} \cdot \mathbf{n} = \alpha(T_{mov} - T_{fix}) + \frac{\eta}{2} \quad \text{on } \Gamma_R(t), \tag{9.6}$$

with α the heat exchange parameter and η a source term due to friction, are applied. Both equations are coupled through the boundary condition on the moving contact line $\Gamma_R(t)$. On the remaining boundaries $\Gamma_{fix,N}$ and $\Gamma_{mov,N}$ a no-flux condition with $\mathbf{n}$ denoting the normal is assumed. Finally $\Omega_{mov}(0) = \Omega_{mov,0}$ and $T_{fix} = T_{mov} = T_0$ for the moving part and the temperatures are used as initial conditions respectively.

9.2.2 Spatial Discretization for Contact Problem in a Simplified Geometry

9.2.2.1 The Diffuse-Domain Method

A phase-field representation of the geometry is constructed in each time step and an implicit mesh defined in the larger box-domain Ω^{dd}, with an adapted grid resolution according to the position of the spindle. Three different were considered phase-field variables, one for the column ϕ_{fix}, one for the spindle $\phi_{mov}(t)$, and one for the

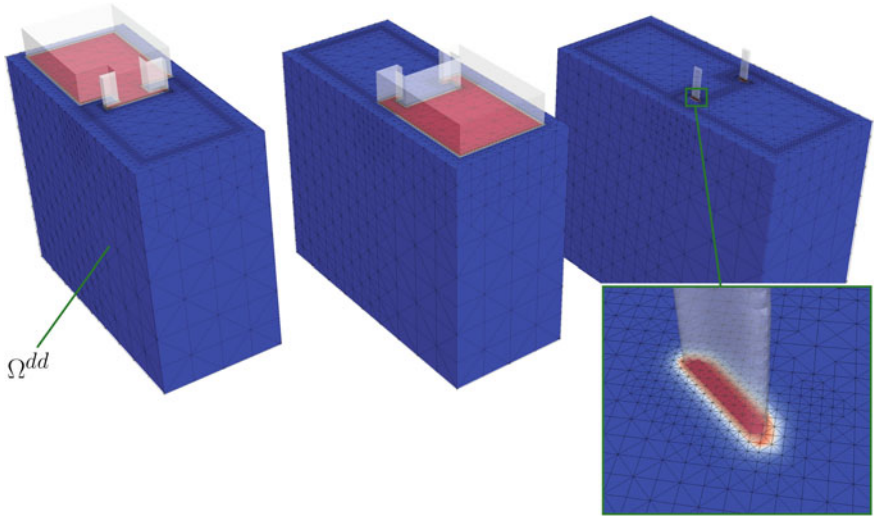

Fig. 9.2 Three clips through the implicit mesh showing the phase-fields for the column (*left*), the spindle (*middle*) and the interface between both parts (*right*). In each of the three pictures the respective component is shown by a transparent *grey* 0,5-contour. The mesh has approximately 1,2 Mio elements, the smallest edge is approximately 1.7 cm. Due to refinement and coarsening the number of elements remains almost constant during the simulation

boundary, where both domains are in contact $\phi_{bnd}(t)$. ϕ_{fix} and $\phi_{mov}(t)$ are defined according to

$$\phi(\mathbf{x},t) := \frac{1}{2}\left(1 - \tanh\left(\frac{3r(\mathbf{x},t)}{\varepsilon}\right)\right), \tag{9.7}$$

where $r(\mathbf{x},t)$ is the signed distance function to $\partial\Omega_{fix}$ or $\partial\Omega_{mov}(t)$. ε is the length scale determining the width of the diffuse interface. $\phi_{bnd}(t)$ results as the product of ϕ_{fix} and $\phi_{mov}(t)$. Figure 9.2 shows the three phase-field functions on distinct clips of the implicit mesh in $\Omega^{dd} = [0,400] \times [0,900] \times [0,900]$ in cm.

All quantities are extended to Ω^{dd} and the diffuse domain approximation is specified as

$$\rho c_p \phi_{fix} \partial_t T_{fix} - k\nabla \cdot (\phi_{fix} \nabla T_{fix}) + \frac{1}{\varepsilon} B(\phi_{bnd})(\alpha(T_{fix} - T_{mov}) + \frac{\eta}{2}) = 0 \tag{9.8}$$

$$\begin{aligned} \rho c_p(\partial_t(\phi_{mov} T_{mov}) + \nabla \cdot (\phi_{mov} \mathbf{v} T_{mov})) - k\nabla \cdot (\phi_{mov} \nabla T_{mov}) \\ + \frac{1}{\varepsilon} B(\phi_{bnd})(\alpha(T_{mov} - T_{fix}) + \frac{\eta}{2}) = 0 \end{aligned} \tag{9.9}$$

in $\Omega^{dd} \cdot \varepsilon^{-1} B(\phi_{bnd}) = \varepsilon^{-1} \phi_{bnd}^2 (1 - \phi_{bnd})^2$ serves as an approximation for the delta-function of Γ_R. The initial conditions are specified as $\nabla T_{fix} \cdot \mathbf{n} = \nabla T_{mov} \cdot \mathbf{n} = 0$ on $\partial\Omega^{dd}$ and $T_{fix} = T_{mov} = T_0$.

9.2.2.2 Explicit Contact Formulation

The two coupled heat transfer equations (9.1) and (9.2) with their corresponding boundary conditions (9.3) to (9.6) are discretized independently of each other by means of linear finite elements in space. They appear in the corresponding weak formulation

$$
\begin{aligned}
T_{fix}(x,t) &= \sum_i T_{fix,i}(t)\varphi_{fix,i}(x) \\
T_{mov}(x(t),t) &= \sum_i T_{mov,i}(t)\varphi_{mov,i}(x(t),t) \\
\forall j : \rho c_p \left(\partial_t T_{fix}, \varphi_{fix,j}\right) + k\left(\nabla T_{fix}, \nabla \varphi_{fix,j}\right) &= \left(\frac{\eta}{2} + \alpha\left(T_{fix} - T_{mov}\right), \varphi_{fix,j}\right)_{\Gamma_R(t)} \\
\forall j : \rho c_p \left(\partial_t T_{mov}, \varphi_{mov,j}\right) + k\left(\nabla T_{mov}, \nabla \varphi_{mov,j}\right) &= \left(\frac{\eta}{2} + \alpha\left(T_{mov} - T_{fix}\right), \varphi_{mov,j}\right)_{\Gamma_R(t)}
\end{aligned}
$$

with the test functions φ_{mov} and φ_{fix} as well as the commonly used L^2-scalar product $(f,g) = \int_\Omega f\, g dx$ with $\Omega = \Omega_{fix}, \Omega_{mov}$. The difficulty arises from the approximation of the boundary integrals and the coupling of T_{mov} and T_{fix} at the contact area.

The time dependency of the boundary integration area is represented by means of the time dependent indicator function

$$
S(t,x) = \begin{cases} 1 & x \in \Gamma_R(t) \\ 0 & \text{else} \end{cases} .
$$

Thus the boundary integrals are extended to the whole frictional boundary $\Gamma_R = \bigcup_{t\in[0,\infty]} \Gamma_R(t)$, independent of the time.

The corresponding boundary integrals

$$
\begin{aligned}
\left(\frac{\eta}{2} + \alpha(T_{fix} - T_{mov}), \varphi_{fix,j}\right)_{\Gamma_R(t)} &= \left(S(t,x)\left(\frac{\eta}{2} + \alpha(T_{fix} - T_{mov})\right), \varphi_{fix,j}\right)_{\Gamma_R} \\
&= \left(F(t,x), \varphi_{fix,j}\right)_{\Gamma_R}
\end{aligned}
$$

now only contain the time dependent non-linear function $F(t,x)$. This function includes the temperature difference $T_{mov} - T_{fix}$, whose evaluation is illustrated in Fig. 9.3 for the example of $T_{fix}(c_i)$ on the moved boundary of Ω_{mov}. The value of

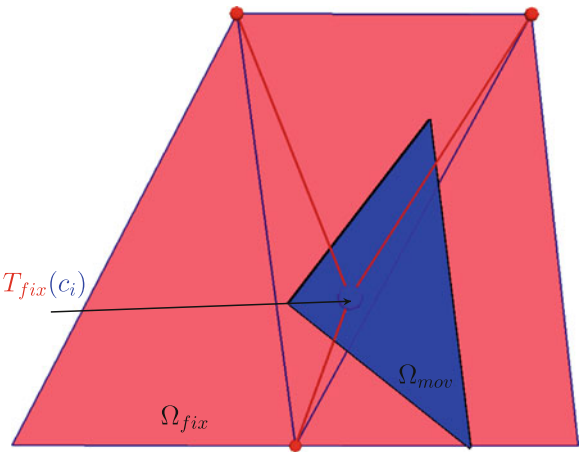

Fig. 9.3 Interpolation of the solutions fo Ω_{fix} (*red*) in the quadrature point c_i of the moved grid Ω_{mov} (*blue*) at the contact area

T_{fix} at the quadrature point c_i is determined by the interpolation of the basis functions on Ω_{fix}.

Spatial discretization followed by the special processing of the contact boundary condition produces an ordinary differential equation of the type

$$\begin{pmatrix} M_{fix} & 0 \\ 0 & M_{mov} \end{pmatrix} \begin{pmatrix} T_{fix} \\ T_{mov} \end{pmatrix} = \begin{pmatrix} A_{11}(t)\, A_{12}(t) \\ A_{21}(t)\, A_{22}(t) \end{pmatrix} \begin{pmatrix} T_{fix} \\ T_{mov} \end{pmatrix} + \begin{pmatrix} G_1(t) \\ G_2(t) \end{pmatrix} \tag{9.10}$$

including the mass matrices M_{fix} and M_{mov}, the time dependent stiffness matrices A_{ij} and the friction terms $G_j(t)$. The resulting system of ordinary differential equations is solved by suitable time integration techniques. Because this is a stiff problem, implicit techniques have to be employed. The Rosenbrock methods have particularly proved to be the method of choice.

9.2.3 *Efficient Long-Term Integration of the Column Geometry*

9.2.3.1 Defect Corrected Averaging

When interpreting the thermal or thermo-elastic machine tool simulation according to the method of lines, then, after having performed the spatial discretization, an ordinary differential equation (9.10) is obtained. A notable feature in the case of the spatially discretized machine tool is a periodic source term on the right side, whereas the period is very short versus temporal horizon of simulation. It is costly and labour-intensive to subject the problem to long-term integration with simultaneous resolution of the small timescale, which, in turn, is dictated by the period

itself. With the method of defect corrected averaging engineered by the authors, it is possible to reach a solution in large time intervals with significantly less calculation time thanks to the use of longer increments. In the following sections, this methodology is introduced when applied to ordinary differential equations of the form

$$\mathbf{y}'(t) = L\mathbf{y}(t) + \mathbf{f}(t), \quad y(0) = y_0 \tag{9.11}$$

In this equation, Ly results from the spatial discretization of an elliptic differential operator, and the discretized source $\mathbf{f}(t)$ is periodical with period ε, that is, $\mathbf{f}(t+\varepsilon) = \mathbf{f}(t)$.

A promising approach consists of replacing the source terms by averaging over a period. Simple averaging, however, leads to solutions that are relatively inaccurate. Defect corrected averaging, in turn, is similar to the concept of stroboscopic averaging by Calvo et al. (2011) and defines a replacement problem, which can be solved with large time increments. The replacement problem is defined so that its exact solution in the stroboscopic points $t = n\varepsilon$ largely conform to the exact solution of the initial problem. The discretized differential operator L remains unchanged here, and the right side $\mathbf{f}(t)$ is replaced by a constant $\mathbf{v}$.

The strategy is illustrated in Fig. 9.4. The highly oscillating solution of the initial problem is marked by circle symbols in the stroboscopic points. The solution by means of simple averaging is a coarse approximation in the stroboscopic points (triangle symbols). The solution of the replacement problem approximates the solution of the initial problem in the stroboscopic points at high accuracy (Fig. 9.5).

Let $S(t_0, t_1, \mathbf{y}_0, \mathbf{f})$ be the solution operator of the differential equation (9.11) with the source $\mathbf{f}(t)$, meaning that the solution in t_1 yields $\mathbf{y}(t1) = S(t0, t1, \mathbf{y}_0, \mathbf{f})$ for

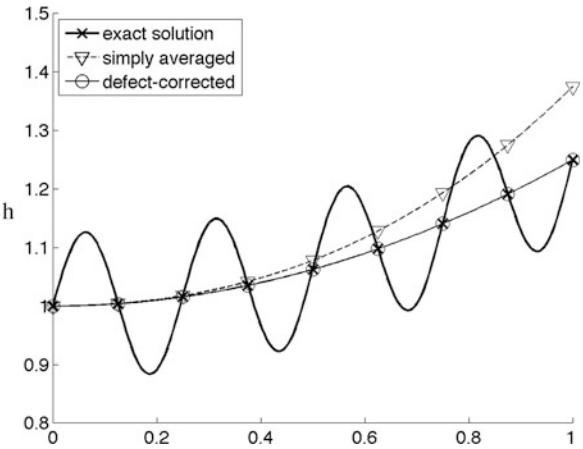

Fig. 9.4 Principle approach in defect corrected averaging: the exact solution (*bold*) is significantly better approximated in the stroboscopic points (*circle symbol*) by defect corrected averaging (*cross symbol*) rather than by simple averaging (*triangle symbol*)

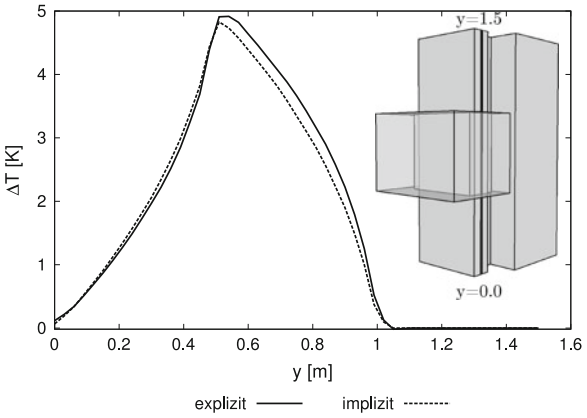

Fig. 9.5 Comparison of reference grid temperature with the diffuse domain solution along the line on Ω_{fix}

$\mathbf{y}(t0) = \mathbf{y}_0$. For a constant source term $\mathbf{f}(t) = \mathbf{v}$, the solution is represented (see Strehmel and Weiner 1982) as

$$S(t_0, t_0 + t, y_0, \mathbf{f}) = \exp(tL)y_0 + t\phi_1(tL)\mathbf{v}, \text{with } \phi(z) = (e^z - 1)/z. \tag{9.12}$$

$$S(0, n\varepsilon, y_0, \mathbf{v}) = S(0, n\varepsilon, (n+1)\varepsilon, y_0, \mathbf{v}) \forall y_0, \forall n \in \mathbf{N}. \tag{9.13}$$

is required for the constant replacement source $\mathbf{f}(t) = \mathbf{v}$. Utilising the following properties of the solution operator

$$S(0, t_1, \mathbf{y}_0, \mathbf{f}(t)) = S(0, t_1, \mathbf{y}_0, 0) + S(0, t_1, 0, \mathbf{f}(t)) \tag{9.14}$$

$$S(0, t_1, 0, \mathbf{f}_1 + \mathbf{f}_2) = S(0, t_1, 0, \mathbf{f}_1) + S(0, t_1, 0, \mathbf{f}_2). \tag{9.15}$$

Equation (9.13) is reduced to

$$S(0, \varepsilon, 0, \mathbf{v}) = S(0, \varepsilon, 0, f(t)), \tag{9.16}$$

whereby only $S(0, n\varepsilon, 0, \mathbf{v}) = t\phi_1(tL)\mathbf{v}$ is valid exactly.

A more in-depth consideration of this relation discloses the structure of the ordinary differential equation (ODE). The solution of the ODE with the periodic source over a time interval ε is on the right side. On the left side, we find a solution with the unknown source $\mathbf{v}$. On the left side, a linear operator affects the unknown $\mathbf{v}$. The coefficients of the corresponding matrix are unknown, but the matrix-vector product can be evaluated by solving the ODE numerically over an interval of ε. In other words: A linear equation system $A\mathbf{x} = \mathbf{b}$ has to be solved, in which the coefficients of A are unknown, whereas the products $A\mathbf{x}$ can be calculated. This is the standard situation for the application of (in which .. are used) Krylov solvers. The Krylov method GMRES according to Saad and Schultz (1986) is used here.

The algorithm to calculate a solution in $t = t_e = n\varepsilon$ is described as follows:

1. Determine $\mathbf{b} = S(0, \varepsilon, 0, \mathbf{f})$ with sufficient accuracy by means of a small-scale integrator.
2. Solve $S(0, \varepsilon, 0, \mathbf{v}) = \mathbf{b}$ by means of GMRES, whereby $S(0, \varepsilon, 0, \mathbf{v})$ is calculated with the small-scale integrator.
3. Solve $y' = Ly + \mathbf{v}$ by means of a suitable large-scale integrator in $[0, t_e]$.

When the solution is to be computed not only at the final point $t_e = n\varepsilon$, but also at other stroboscopic points $t_0 \in (0, t_e)$, then it is possible to choose the incremental steps of the large-scale integrator. If the solution also has to be found for non-stroboscopic points t_i, then it is necessary to determine the solution by means of the large-scale integrator at the first previous stroboscopic point, and to subsequently achieve the solution at t_i, by means of a small scale integrator. The method is very efficient, if the solution is sought at a few selected points on a large time scale.

As practical tests show, it is possible to enhance the convergence of the GMRES iteration when initialising with an averaging of the sources over a period so that it is only necessary to correct the defect between the exact solution and the solution which has been achieved through simple averaging over a period. Tests for this simple defect corrected averaging by Naumann and Wensch (2013) enhance defect reduction by a factor of 100 in comparison with simple averaging. Preconditioners, which offer an opportunity for further acceleration of computation, are introduced in Sect. 9.2.4.2.

9.2.3.2 Preconditioning in Defect Corrected Averaging

Our problem consists in the solution of the linear equation system

$$A\mathbf{x} = b \tag{9.17}$$

whereby matrix A results from the spatially discretized differential operator L through

$$A = \varepsilon\phi_1(\varepsilon L) = \varepsilon\frac{\varepsilon L - 1}{\varepsilon L}. \tag{9.18}$$

A good preconditioner P is an approximation of the inverse of matrix A, whereby the condition of P should be significantly less than the condition of A. For this purpose, the authors employ Pade approximations $R(z)$ of the function $\phi_1(z)^{-1}$ in $z = 0$, but, additionally, we demand the same asymptotic behaviour. The resulting preconditioner is $P = R(L)$. Since ϕ^{-1} shows for $z \to -\infty$ the same asymptotic behaviour as $-z$, then $p = q + 1$, with p as the degree of numerator and q as the degree of denominator. This results in $2q$ degrees of freedom, one of which is used for the asymptote at $-\infty$, and the others for the adjustment of the derivates in $z = 0$. This means that one can adjust $2q - 1$ derivates in $z = 0$.

The variants $q = 0$ and $q = 1$ yield:

1. R linear, $R(0) = \phi_1(0)^{-1}$

$$R(z) = -\frac{z}{2} + 1.$$

2. R is a rational fraction, degree of numerator 2, degree of denominator 1

$$R(z) = \frac{z^2 - 2z + 2}{-z + 2}$$

These preconditioners make the defect corrected averaging significantly more efficient and allow for an exact solution for large oscillating ODEs on large time scales.

9.3 Results

9.3.1 Comparison of the Diffuse-Domain Method with Explicit Formulation of the Contact

The two approaches described under Sects. 9.2.2.1 and 9.2.2.2 were compared in terms of computation accuracy and run time characteristics. First, the convergence behaviour of the explicit formulation of the contact was explored. To do this, 3 adaptively refined grids were used. The basic grid in Fig. 9.6 was refined along the heating boundary so that the grid width is halved in this area. To calculate the

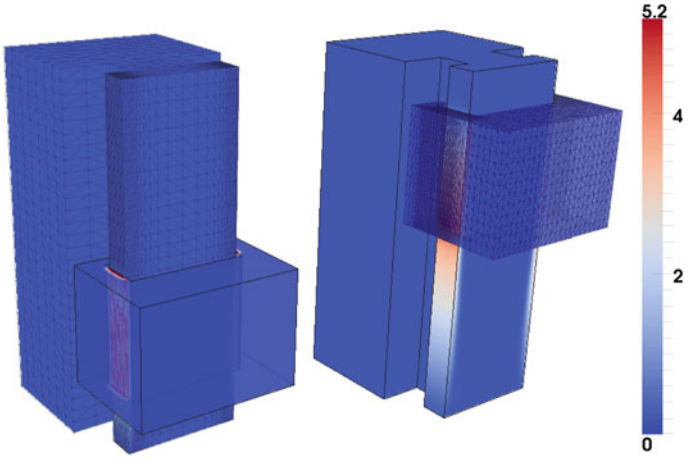

Fig. 9.6 Temperature on the explicit grid with the formulation of the contact at the times 6 and 20 s

Table 9.2 Accuracy and convergence behaviour of the explicit solution at time $t = 12$

$\|T_{\delta t,h} - T_{ref}\|_2$	h	h/2	$EOC_{\delta t}(h)$
24/80	0.005	0.003	0.6
24/160	0.003	0.002	1.1
24/320	0.003	0.001	1.6
$EOC_h(\delta t)$	0.5	1	1.9

reference solution, the time stepsize $\delta t = 24/320$ and the basic grid refined twice from Fig. 9.6 were used. The temperatures were compared at the point of t = 12 s. At this point, the spindle head is in the half-height position. The accuracy of the explicit simulation is shown in Table 9.2.

The solutions of the explicit discretization are compared not only with the time stepsizes 24/80, 24/160 and 24/320, but also with the basic grid and the grid refined once with the reference solution in the L^2 norm. For sufficiently fine grids, the defect behaviour, shown in Table 9.2, corresponds to the theoretical prediction of the implicit Euler method used. On the basic grid, however, the spatial defect dominates.

The convergence behaviour of the diffuse domain method has already been explored in Franz et al. (2012) and shows quadratic convergence in ε.

For validation, the one-time motion of the spindle head upward is simulated. After each time step, the implicit grid is adapted to the moved geometry. After 81 time increments, the spindle head reaches the upper end of the machine column. Figures 9.7 and 9.6 show the temperature distribution on the subassembly's surface by means of the diffuse domain method and explicit discretization at two different simulation times. The parameters $\rho = 7.200$ kg/m^3, $C_p = 460$ kJ/(kg K),

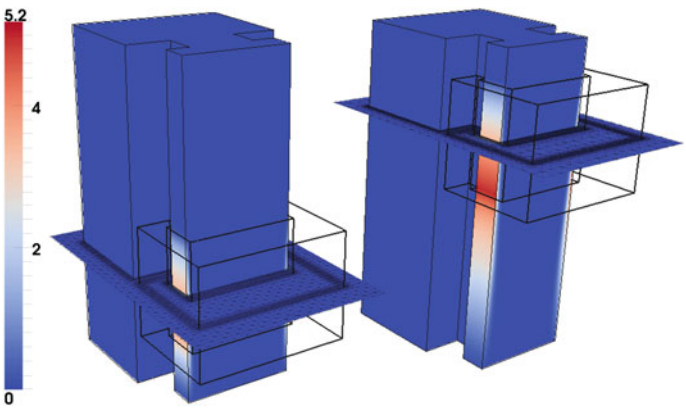

Fig. 9.7 Temperature field on the implicit grid by means of the diffuse domain method (sectional plane) the times 6 and 20 s

$k = 50,000$ kW/(km), $\alpha = 100$ W/K, $\theta = 17.1875$ J and $v = 0.041667$ m/s were used. The interface width was $\varepsilon = 0.2$ m.

The reference solution for the explicit coupling and the diffuse domain solution described were used to compare both methods. Temperature is shown in Fig. 9.5 along the black line on the frictional boundary. Both temperature curves are qualitatively similar. The offset is approximately equal to the washing out due to the phase field width ε.

The defect in the L^2-norm over the entire area is 0.0065 and thus in the order of magnitude of the explicit discretization's numerical error, which confirms the usability of the diffuse domain method. It took about 36 h to carry out the simulation with the diffuse domain method, but only 72 min to perform the explicit formulation of the contact for 320 time increments. The long runtime requirements are caused by the substantially higher number of degrees of freedom. The significant advantage of the approach, which is founded on rapid and simple grid generation and the usability of standard routines, is thus nullified again by the increased runtime demand again. This becomes more obvious when using the original geometry and process conditions. In the following, the explicit formulation of the contact boundary condition was employed.

In both paradigms, the finite element discretization was performed by means of the parallel adaptive finite element library AMDiS by Vey and Voigt (2007), Voigt and Witkowski (2012), however, were used in the sequential mode.

9.3.2 Results of Defect Corrected Averaging

The method was used in order to simulate the thermo-elastic behaviour of the column/spindle configuration in its complex geometry over a period of 15 h. This problem was regarded as the reference problem to evaluate and benchmark the MOR techniques developed under A05 and A06. The periodic source is given here by the frictional heat at the periodically moved contact position. For the whole boundary, heterogeneous Robin boundary conditions are used, which represent the ambient cooling. In this time span, 75–2,400 periodical motions are executed per hour. The solution calculated by means of the small scale indicator was used as reference solution. The comparison involves the solutions with simple averaging and defect corrected averaging, where the latter was used with preconditioner. The results in Table 9.3 demonstrate that defect correction enhances simple averaging.

Table 9.3 Runtime versus accuracy—compared for different averaging methods

Method	Runtime	Error (K)
Small scale integration	72 h	
Simple averaging	3 min	0.25
Defect corr. averaging with preconditioning	22 min	0.025

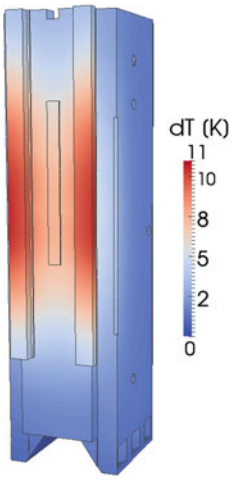

Fig. 9.8 Temperaturfeld mit defektkorrigierter Mittelung nach 15 h

The cost of this advantage is an increased calculation time; however, this is still lower by some orders of magnitude than in small scale simulation. In this simulation, one third of the correction effort results from the application of the preconditioned GMRES, and the other two thirds from the calculation of the right side with 100 steps. After simulation of the thermal behaviour, the temperature fields are employed to determine the corresponding deformations from linear elasticity.

The combination of the two approaches permits an efficient simulation of the machine tool with its moving subassemblies. Figures 9.8 and 9.9 illustrate the calculated temperature fields and the amount of deformation in the original geometry with the given, varying periods after 15 h. The calculation is also carried out in AMDiS.

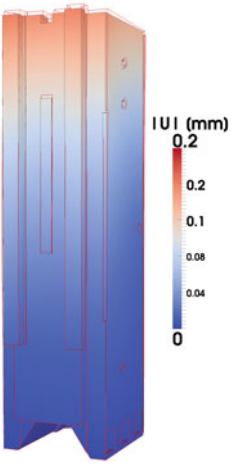

Fig. 9.9 Absolutwert der Verschiebungen nach 15 h. Die roten Linien entsprechen der deformierten Geometrie mit 100 facher Verstärkung der Verschiebungen

Figure 9.9 clearly shows the strongest heating at the frictional boundary; the difference in temperature is here 11 K. In the correspondent right Fig. 9.9, the absolute displacement is shown. The red lines represent the deformed geometry, with the deformation amplified by a factor of 200 for visualisation. A detailed comparison of the simulation results with the subprojects A05 and A06 and the measurements gained in experiments is now underway.

9.4 Classification in the CRC/TR 96

In subproject A07, different mathematical methods for the simulation of the thermo-elastic machine tool behaviour were investigated. Coupling strategies for finite element spaces moved against each other were developed to simulate thermo-elasticity in moving geometries. The interpolation algorithm applied here provided exact results and is used to generate reference solutions for other subprojects. As an alternative, the diffuse domain approach was tested. This approach provides similar results and permits the use of standard methods and an easy processing of geometries, but suffers, however, from substantially longer computer runtime. The high resolution reference solutions generated contribute to the validation of the numerical results obtained using the commercial software packages in A05 and the results of the model reduction methods in A06. The comparisons (benchmarks) will be published elsewhere.

9.5 Outlook

Defect corrected averaging was developed and further refined by preconditioning techniques for the simulation over long time intervals, in which periodic motions appear over large partial intervals. This method makes possible efficient simulation over very long time intervals and is significantly more accurate than simple averaging techniques. An additional strength is that it is substantially faster than a simulation on the small time scale of periodic motions. After successful processing of spatial discretization, the focus is on further improvement of time discretization. At the time of publication, the method is being expanded by the Robin boundary conditions that they are needed in subproject A05. In the next phase, temporal integration methods that can be paralleled will be used in order to carry out simulations more efficiently over greater time spans. The methods of choice in terms of the structure of the thermo-elastic FE models are the approaches by ParaReal (Nielsen 2012), as well as ParaExp (Gander and Güttel 2013).

References

Calvo MP, Chartier P, Murua A, Sanz-Serna JM (2011) Numerical stroboscopic averaging for ODEs and DAEs. Appl Numer Math 61(10):1077–1095. doi:10.1016/j.apnum.2011.06.007. http://dx.doi.org/10.1016/j.apnum.2011.06.007

Franz S, Gärtner R, Roos H, Voigt A (2012) A note on the convergence analysis of a diffuse-domain approach. Comp Meth Appl Math 12:153–167

Gander MJ, Güttel S (2013) Paraexp: A parallel integrator for linear initial-value problems. SIAM J. Scientific Computing

Li X, Lowengrub J, Raetz A, Voigt A (2009) Solving pde's in complex geometries: a diffuse domain approach. Commun Math Sci 7:81–107

Naumann A, Wensch J (2013) Defect corrected averaging for highly oscillatory pdes. PAMM (accepted for publication)

Nielsen AS (2012) Feasibility study of the parareal algorithm. Master's thesis, Technical University of Denmark, DTU Informatics, E-mail: reception@imm.dtu.dk, Asmussens Alle, Building 305, DK-2800 Kgs. Lyngby, Denmark. http://www.imm.dtu.dk/English.aspx, DTU supervisor: Allan P. Engsig Karup, apek@imm.dtu.dk, DTU Informatics

Saad Y, Schultz M (1986) GMRES: a generalized minimal residual algorithm for solving nonsymmetric linear systems. SIAM J Sci Stat Comput 7:856–869

Strehmel K, Weiner R (1982) Behandlung steifer Anfangswertprobleme gewöhnlicher Differentialgleichungen mit adaptiven Runge-Kutta-Methoden. Computing 29:153–165

Vey S, Voigt A (2007) AMDiS: adaptive multidimensional simulations. Comput Vis Sci 10 (1):57–67. http://dx.doi.org/10.1007/s00791-006-0048-3

Voigt A, Witkowski T (2012) A multi-mesh finite element method for lagrange elements of arbitrary degree. J Comput Sci 3:420–428